Electrochimica Acta 445 (2023) 142056

Contents lists available at ScienceDirect

Electrochimica Acta

journal homepage: www.journals.elsevier.com/electrochimica-acta

Increasing the efficiency and cycle life of Na-O_2 batteries based on graphene cathodes with heteroatom doping

M. Enterría [a], R. Mysyk [a], L. Medinilla [a], S. Villar-Rodil [b], J.I. Paredes [b], I. Rincón [c], F. J. Fernández-Carretero [c], K. Gómez [a], J.M. López del Amo [a], N. Ortiz-Vitoriano [a,d,*]

[a] Center for Cooperative Research on Alternative Energies (CIC energiGUNE), Basque Research and Technology Alliance (BRTA), Alava Technology Park, Albert Einstein 48, 01510, Spain
[b] Instituto de Ciencia y Tecnología del Carbono INCAR-CSIC, C/Francisco Pintado Fe 26, Oviedo 33011, Spain
[c] TECNALIA, Basque Research and Technology Alliance (BRTA), Parque Científico y Tecnológico de Gipuzkoa, Mikeletegi Pasealekua 2, 20009 Donostia-San Sebastián, Spain
[d] Ikerbasque, Basque Foundation for Science, María Díaz de Haro 3, Bilbao 48013, Spain

ARTICLE INFO

Keywords:
Metal-air batteries
Sodium
Graphene
Cycling
Parasitic reactions

ABSTRACT

To overcome the challenges of Na-O_2 batteries with respect to efficiency, capacity, and cycle life as well as to develop cheap, metal-free, and abundant electrocatalysts, we explored boron and nitrogen-functionalized graphene aerogels prepared by the hydrothermal self-assembly of graphene oxide with subsequent thermal reduction. The results showed an improve of both the cycling overpotential and the coulombic efficiency for the functionalized graphene aerogels. However, the nitrogen-containing cathode presented a shortened cycle life and decreased charging stability. The postmortem analysis of the full discharge, and the full discharge and charge cathodes demonstrated that nitrogen functionalization triggered the formation of solid parasitic products that passivate the cathode surface, thus resulting in a poorer electrochemical performance. By contrast, functionalization with boron-containing groups demonstrated to be a more promising strategy due to minimized parasitic products, leading to lower oxygen reduction and evolution overpotentials with a concomitantly enhanced cell efficiency vs. the undoped cathodes. This resulted in a cycle life of 70 cycles at a relatively high current density of 0.1 mA cm^{-2} with a capacity cut-off of 0.5 mAh cm^{-2}. Our study underscores that functionalization with heteroatoms simultaneously alters multiple characteristics of graphene-based materials, including their chemistry, texture and morphology, which in turn presents a critical impact on the electrochemical response of the resultant Na-O_2 cells.

1. Introduction

Rechargeable batteries represent a link between renewable energy sources and mobile applications, particularly portable electronic devices, and electric vehicles. The much-sought transition to a fossil fuel-free economy is tightly linked to further enhancements in essential features of batteries such as energy density, safety, lifetime, temperature range or lower maintenance requirements. As well the use of inexpensive and more environmentally friendly battery components, free of heavy, precious and scarce metals is crucial [1]. Despite lithium-ion batteries (LiB) currently dominate the battery market for electric vehicles and portable devices, they still fall short of providing the autonomy required in other important applications. In addition, the scarcity and limited geographical availability of lithium ores present serious pitfalls to the use of LiB on an increasingly larger scale, especially in the context of full-fledged electromobility growth, requiring tremendously high amounts of Li to be readily available for industry [2]. These considerations have led to alternative battery developments, such as the so-called "beyond lithium-ion" energy storage. In this context, sodium-oxygen (Na-O_2) batteries are of special interest due to their high theoretical energy density exceeding that of LiB by at least a factor of 5 (1108 vs. 265 Wh kg^{-1}). Na–O_2 batteries are chemical conversion devices based on the electrochemical reduction of molecular oxygen [oxygen reduction reaction (ORR)] at the “air cathode” where different

* Corresponding author at: Center for Cooperative Research on Alternative Energies (CIC energiGUNE), Basque Research and Technology Alliance (BRTA), Alava Technology Park, Albert Einstein 48, 01510, Spain.
E-mail address: nortiz@cicenergigune.com (N. Ortiz-Vitoriano).

https://doi.org/10.1016/j.electacta.2023.142056
Received 3 January 2023; Received in revised form 12 February 2023; Accepted 14 February 2023
Available online 18 February 2023

sodium oxides are formed on its surface during discharge. On charge, the discharge products release the molecular oxygen back via the oxygen evolution reaction (OER) [3]. Despite the clear principle, nowadays Na–O_2 batteries are still in early development due to a series of fundamental challenges that need to be understood and resolved before reaching an industrial technology readiness level. In this context, the choice of the optimum cathode material is critically important since it has a direct impact on the kinetics of both ORR and OER. The products and their formation mechanisms depend particularly on the catalytically active surface at the cathode, which has to catalyze the ORR, serving as nucleation sites for the growth of discharge products while making easier their oxidation and redissolution during oxidation (OER) [4–6]. Carbon based cathodes are the material of choice for metal-O_2 batteries in general, and Na–O_2 batteries in particular, thanks to their tunability in terms of surface area, porosity, conductivity, chemical stability, and, most importantly, functional surface chemistry [7]. Graphene stands out among carbon materials thanks to its high electrical conductivity and stable 2D structure. To be suitable for Na-O_2 cells, graphene cathodes must present mechanical stability, favor O_2 diffusion and electrolyte permeation onto active sites for the formation/decomposition of discharge products [8]. In this regard, the strong tendency of the graphene sheets to re-stack (due to van-der-Waals forces) makes it difficult to fabricate mechanically stable and surface accessible materials. The engineering of graphene into 3D structures (i.e. aerogels) is one possible way to address this issue and access suitable graphene-based materials for Na-O_2 battery cathodes [9,10]. In order to enhance the catalytic performance of graphene-based cathodes, functionalization with non-metallic heteroatoms opens sustainable avenues for tuning the ORR and OER [11]. Both theoretical and experimental studies indicate that functionalizing and/or doping carbon-based materials with atoms such as nitrogen, boron, sulfur or phosphorous improve the ORR catalytic activity, which may be attributed to the polarized distribution of spin and charge densities [12]. For instance, it has been reported that the configurations of nitrogen when functionalizing or doping carbon materials have a great influence on the catalytic activity of carbon-based materials. Hence, pyrrolic and pyridinic like groups are though to promote high catalytic activity while quaternary nitrogen is beneficial for improving electronic conductivity. Hierarchical porous carbons have been tailored for nitrogen doping level, pore size distribution, and specific surface area. The functionalization of carbon together with the maximization of the surface area resulted in a greatly lowered cycling overpotential as well as enhanced catalytic activity, discharge capacity, and cycle life over the values measured for the undoped counterpart [13]. A study reported by Zheng et al. using polypyrrole derived nanofiber, annealed to different temperatures, in a glyme based electrolyte, showed that those treated at 700 °C delivered the best electrocatalytic activity for both ORR and OER [14]. This resulted in an enhanced discharge capacity, cycling life (~ 90 cycles at current density of 200 mA g^{-1} with fixed capacity of 500 mAh g^{-1}) and stability due to a carbon structure rich in both pyrrolic and pyridinic groups; unlike other studies with quaternary nitrogen-doped or pyridinic groups. In another study, nitrogen-doped carbon nanotubes showed better electrocatalytic activity and cycle stabilities than undoped nanotubes in a glyme based electrolyte. The authors ascribed this behavior to the nitrogen active sites which enabled fast oxygen reduction processes, leading to a layer-by-layer deposition of the discharge products which covered all the nanotube surface. In contrast, the lack of specific active sites in the bare nanotube led to random deposition of big particles which were difficult to redissolve during charge [15]. Functionalization with elements that are more electropositive than carbon (e.g., boron) are rather scarce in literature. Shu et al. reported a Na–O_2 battery using a mesoporous boron-doped onion-like carbon microspheres where boron doping led to an enhanced oxygen adsorption on the carbon surface which resulted in higher specific capacity, improved rate capability (capacity retention of 73% when the discharge current density increased from 0.15 to 0.60 mA cm^{-2}) and cycling stability (125 cycles at 0.3 mA cm^{-2} with a fixed capacity of 1000 mAh g^{-1}) [16]. The reported structure was also beneficial due to the large amounts of mesopores, and numerous active sites associated with boron doping. Although heteroatom-doped graphene-based materials is a common strategy for energy relevant electrocatalytic processes [17], few studies have been reported for Na-O_2 batteries (unlike carbon materials described above). Li et al. studied nitrogen-doped of graphene nanosheets (GNSs), in a glyme based electrolyte, which improved the catalytic activity relative to the undoped electrodes (e.g. at 75 mA g^{-1} double discharge capacity was attained for the N-doped GNSs (8000 vs 4000 mAh g^{-1}) [18]. In this study however, no cycling data was reported. Benti et al. further study theoretically the role of nitrogen and boron doped graphene, and co-doped graphene as potential catalysts for rechargeable non-aqueous sodium–air batteries. They predicted that single and double-boron-bonded graphene and graphene doped with pyridinic nitrogen should exhibit a lower overpotential for ORR and high OER catalytic activity in non-aqueous Na–O_2 batteries among range of explored doped graphene materials [19]. Due to the lack of fundamental understanding of heteroatom doped graphene in Na-O_2 batteries and the promising results in other energy storage systems, herein, we investigate the role of functionalization of graphene-based materials with functional groups based on either boron or nitrogen. That is, atoms that are more electropositive and electronegative to carbon, respectively, for understanding their roles as cathodes in Na-O_2 batteries. Hydrothermally derived graphene oxide aerogels were functionalized with nitrogen and boron and reduced by thermal treatment to different temperatures under inert atmosphere. The ORR electrocatalytic activity of these materials was investigated in basic aqueous electrolyte. The most promising materials were coated into a porous commercial gas diffusion layer and tested as Na-O_2 battery electrodes, using aprotic electrolyte. Characterization of discharge/charge electrodes was further conducted to analyze the discharge product morphology and chemistry. Moreover, solid and liquid NMR were performed to evaluate the parasitic chemistry and stablish an overall relationship between the phytochemical properties of graphene functionalized air cathodes, electrochemical performance and postmortem characterization.

2. Experimental

2.1. Preparation of functionalized graphene aerogels

The preparation of the graphene aerogels was carried out using commercial graphene oxide (GO) dispersion (4 mg mL^{-1}) supplied by Graphenea. 15 g of GO dispersion were loaded into a teflon lined stainless steel autoclave and heated at 180 °C for 16 h. In the case of nitrogen and boron functionalized aerogels, ammonia was added drop by drop until pH 9 was reached [20] or 38 mg of boric acid [21] were added to the GO dispersion prior to the hydrothermal treatment. The obtained samples were washed three times with deionized water, frozen for 24 h at −80 °C and freeze-dried at −10 °C and 63 Pa for 12 h. The obtained 3D aerogels were thermally reduced in a tubular quartz oven at either 700 or 1000 °C, using a 2 °C min^{-1} heating ramp and Ar inert atmosphere (100 cm^3 min^{-1}). The resulting aerogels were denoted as XrGO Y where X is the heteroatom introduced in the material and Y the temperature of reduction. For instance, rGO 700 is the unfunctionalized material treated up to 700 °C and NrGO 1000 is the nitrogen-functionalized aerogel which was reduced up to 1000 °C.

2.2. Preparation of graphene-based battery cathodes

The cathodes were manufactured by depositing the powdered graphene aerogels prepared in Section 2.1 over a commercial gas diffusion layer (GDL). To that aim, a H23C2 Freudenberg GDL, comprising a carbon fiber paper coated with a microporous carbon black layer, was selected as support. The different graphene aerogel powders and polytetrafluoroethylene (60 wt.% water dispersion from Sigma Aldrich)

were mixed in a 90:10 w/w.% ratio in a mixture of ethanol and water (3:7 w/w.%) and sonicated to different times as function of each material dispersibility. The longest sonication time (4 h) was required for nitrogen functionalizes samples, which presented the poorest dispersibility. In contrast, BrGO 700 and rGO 700 aerogels were correctly dispersed after 2 h of sonication. The thus obtained ink was spread over the surface of the GDL with an automated film coater. Solvent was left evaporating at room temperature overnight and then the coated GDL were placed into a vacuum oven at 50 °C for 24 h.

2.3. Physicochemical characterization of graphene aerogel powders, pristine cathodes and full discharged or charged cathodes

The porosity, chemical composition and surface chemistry of powdered graphene aerogels were characterized by low-temperature nitrogen adsorption, elemental analysis (EA), and X-ray photoelectron spectroscopy (XPS). Nitrogen adsorption isotherms were measured at −196 °C using a Micromeritics ASAP 2020 instrument for relative pressures (P/P_0) between ~10^{-8} and 0.995. Samples were preliminarily outgassed for 24 h at 200 °C. The specific surface area and pore size distribution were calculated by applying Brunauer-Emmett-Teller (BET) [22] and 2D Non-Local Density Functional Theory (2D NLDFT, data reduction software SAEIUS) [23] to the obtained isotherms. The total pore volume was calculated by the amount of adsorbed gas at P/P_0=0.99. The quantification of carbon and hydrogen by EA was done in a LECO CHN-2000 instrument, whereas oxygen and sulfur were measured with a LECO Truspec Micro O accessory and a LECO S632 analyzer, respectively. Carbon, hydrogen and sulfur were determined, respectively, from the amount of CO_2, H_2O and SO_2 generated upon combustion of the sample, and oxygen was inferred from the amount of CO and CO_2 produced upon its pyrolysis at high temperature. Samples were dried overnight at 100 °C prior to elemental analysis. XPS was performed on a SPECS spectrometer equipped with a Phoibos 100 hemispherical electron energy analyzer. The spectra were acquired at a pressure below 10^{-7} Pa using a monochromatic Al K_α X-ray source operated at a voltage of 14.00 KV and a power of 175 W. The photo-excited electrons were analyzed in constant pass energy mode, using pass energy of 50 and 10 eV for the survey and the high-resolution core level spectra, respectively. Spectra were recorded at a take-off angle of 90°. The XPS data were analyzed using CasaXPS software. The compositions in weight percentage (wt.%) were determined from the survey spectra by considering the integrated peak areas (after corrections for the mean free path of the outgoing electrons and the transmission function of the analyzer) of the main XPS peaks of different elements and their respective sensitivity factors. Core level curve fitting in different components was performed using a Shirley background and a standard least squares algorithm. Each component was considered as a convolution of a Gaussian and a Lorentzian function (80:20). The surface of pristine, discharged and cycled graphene-GDL cathodes was inspected by scanning electron microscopy (SEM), Raman and Nuclear Magnetic Resonance (NMR) spectroscopies. In the case of postmortem analysis, the battery cells assembled as described in Section 2.4, were opened inside an Ar-filled glove box. The different cathodes were washed with ethylene glycol dimethyl ether (DME) to remove the excess of salt, dried and transferred to the characterization equipment using an air-tight holder to avoid the degradation of the air/moisture sensitive products. The morphology, particle size and particle distribution of these discharge products was studied by using a FEI Quanta 250 microscope operating at 20 kV. The chemical nature of discharge products formed in the surface of the different cathodes was studied by Raman spectroscopy in a Renishaw spectrometer (Nanonics Multiview 2000) operating with an excitation wavelength of 532 nm. The spectra were obtained by performing 5 acquisitions with 30 s of dwell time. Postmortem analysis of the cathodes was also conducted by a combination of liquid and solid-state Nuclear Magnetic Resonance (NMR). Solid-state experiments were conducted at a 500 MHz WB spectrometer while liquid-state characterizations were carried out at a 300 MHz SB magnet. The insoluble solid discharge products present on the surface of either full discharge or full discharged/charged cathodes were characterized by ^{23}Na solid state NMR. The discharged electrodes were cut into pieces and packed into 2.5 mm diameter MAS rotors inside an argon glove box. ^{23}Na solid-state NMR spectra were acquired using 1.5 μs π/2 excitation pulses, a recycle delay of 2 s and up to 15k scans acquired depending on the signal to noise. ^{23}Na chemical shifts were referenced to a 0.1 M NaCl solution at 0 ppm. All spectra were collected at a MAS rate of 20 KHz at room temperature. NMR experiments in solution were performed at 30 °C on a 300 Bruker AVANCE III HD spectrometer under Topspin 3.5 and equipped with a Bruker BBFO z-gradient 5 mm probe head. All samples were acquired with 128 transients, a spectral width of 6009.6 Hz, recycle delay of 1.0 s, acquisition time of 5.45 s, 90° pulse of 14 μs, and 64 K data points. The discharge electrodes were soaked in DMSO-d^6 99.8% (Eurisotop) for 15 h, filtered and the obtained solutions were analyzed by 1D and 2D experiments.y pano

2.4. Assessment of the ORR electrocatalytic performance of graphene aerogels

The electrocatalytic activity towards ORR of the reduced graphene oxide aerogels was investigated using a Rotating Disk Electrode (RDE) with an ALS RRDE-3A miniature rotator coupled to a Biologic VMP-3 potentiostat. The experiments were carried out in a three-electrode configuration cell, using an O_2-saturated 1 M KOH solution as electrolyte, a Pt wire counter electrode and a reversible hydrogen electrode (RHE) as reference. Alkaline media was chosen for the experiments as a tool to evaluate the initial performance of the air cathodes based on previous studies in literature and due to the challenging set-up of performing these studies in organic media (no contact with air) [24,25]. The working electrodes were prepared by the deposition of ~ 2.38 μg (equivalent of 5 μL of graphene dispersion) on a glassy carbon disk with a surface area of 0.07 cm^{-2}. A continuous catalyst layer was deposited onto the glassy carbon electrode by adding the dispersion drop by drop, letting the solvent to evaporate between each droplet. The suspensions were prepared by dispersing 4.8 mg of graphene and a 100 μL of a 5% wt Nafion dispersion (Sigma-Aldrich) in a solution of 7.6 ml of water and 2.4 ml of isopropanol. The suspension was sonicated for 4 h (NrGO 700) or 2 h (rGO 700 and BrGO 700) until homogeneous ink was obtained. The mass loading of the samples was ~0.034 mg $cm^{-2.}$ The electrolyte solution was saturated in O_2 for 30 min prior to the electrochemical measurements. Linear sweep voltammetry (LSV) curves were registered at a scan rate of 20 mV s^{-1} a rotation speed of 400, 625, 900, 1225, 1600 and 2500 rpm and a voltage window from 0.326 to 0.826 V vs RHE. The background LSV curves under Ar atmosphere were recorded and subtracted from those obtained under oxygen atmosphere. The ORR onset potential (E_{onset}) was determined by taking the value at the intersection point between two tangents in the current density vs potential plot; (1) the plateau at higher voltages (non-faradaic or capacitive region) and (2) the maximum slope on the region where a current density starts to decrease due to the occurrence of a faradaic process (effective transfer of electrons). To further elucidate the ORR kinetics, LSV curves at different rotation speeds, ranging from 400 to 2500 rpm, were acquired and the Koutecky-Levich equations were employed to obtain the electron transfer number [26]:

$$\frac{1}{j} = \frac{1}{j_k} + \frac{1}{j_D} \tag{1}$$

$$j_D = 0.62nF(D_0)^{2/3}\nu^{-1/6}C_0\omega^{1/2} = B\omega^{1/2} \tag{2}$$

$$j_K = nFKC_0 \tag{3}$$

where j is the measured current, j_k the kinetic current, j_D the diffusion limited current, n represents the number of electrons transferred per

oxygen molecule, F is the Faraday constant ($F = 96{,}485$ C mol^{-1}), D_0 is the diffusion coefficient of O_2 in 1 M KOH (1.9×10^{-5} cm^2 s^{-1}), ν is the kinetic viscosity (0.01 cm^2 s^{-1}), C_0 is the bulk concentration of O_2 (1.2×10^{-6} mol cm^{-3}), ω is the rotation speed in rad s^{-1} and K is the electron transfer rate. The value of transferred electrons (n) and the electron transfer rate (K) is obtained by combining Eq. (1) with (2) and (3), from the slope and intercept of the J^{-1} vs. $w^{-1/2}$ plot, respectively.

$$\frac{1}{j} = \frac{1}{j_k} + \frac{1}{B\omega^{1/2}} \tag{4}$$

2.5. Evaluation of the electrochemical performance of the graphene cathodes on a Na-O_2 cell

A pressurized 2-electrode Swagelok-type cell was used for galvanostatic measurements. The cells were dried overnight and transferred to an Ar-filled glove box ($H_2O < 0.1$ ppm, $O_2 < 0.1$ ppm, Jacomex, France). The electrolyte was prepared using ethylene glycol dimethyl ether solvent (DME, anhydrous, 99.5% Sigma Aldrich) preliminarily dried over molecular sieves (3 Å, Sigma Aldrich) for one week. Sodium trifluoromethanesulfonate (CF_3NaO_3S or NaOTf, 99.5%, Solvionic) was employed as a conductive salt after drying under vacuum at 120 °C for 24 h. 0.5 M NaOTf in DME was prepared by vigorously stirring the mixture of the conductive salts and solvent. The electrolyte solutions prepared in the glove box presented water content values below 8 ppm (as determined by a C20 Karl Fisher coulometer, Mettler Toledo). The catalyst layer on the GDL type cathodes prepared as described in Section 2.2 were put over a stainless-steel mesh (1.13 cm^2, Alfa Aesar) which was used as porous current collector. Celgard H2010 was employed as a separator and a sodium disk (0.95 cm^2) as both reference and counter electrodes. The assembled cells were pressurized with pure oxygen to ≈1 atm and left to rest for 8 h at an open circuit voltage (≈2.2–2.3 V vs Na/Na$^+$) before electroanalytical runs. Galvanostatic full discharge, full charge-discharge cycle and shallow cycling measurements were performed using a Biologic-SAS VMP3 potentiostat at a current density of 0.2 mA cm^{-2} in a potential range of 1.8–3.2 V versus Na/Na$^+$.

3. Results and discussion

3.1. Assessment of the ORR electrocatalytic performance of the graphene aerogels in aqueous electrolyte by RDE

The current density in the LSV curves for the different graphene-based cathodes, in O_2-saturated 1 M KOH electrolyte, presented a linear relationship with the rotation speed (Fig. S1), suggesting a diffusion-limited electron transfer. Bearing this in mind, a high rotation rate of 2500 rpm was selected to compare the different LSV curves as a function of the graphene-based catalyst in Fig. 1. The potential where the current density starts to decline in the anodic potential sweep is known as onset potential (E_{onset}), where a higher value indicates a better electrocatalytic activity towards the ORR reaction. This parameter was determined from the LSV curves and listed in Table 1. The ORR onset for the pristine rGO and rGO 700 was similar (0.758 V vs RHE) and was lower for rGO 1000 (0.736 V vs RHE), indicating a decreased electrochemical activity for the later sample Fig. 1a). In case of the BrGO series, the value decreased gradually with the increase of the treatment temperature from BrGO (0.767 V vs RHE) to BrGO 1000 (0.747 V vs RHE) (Fig. 1c). The highest ORR onset potential was exhibited by both the as-prepared NrGO and NrGO 700 aerogels (0.799 V vs RHE) whereas that

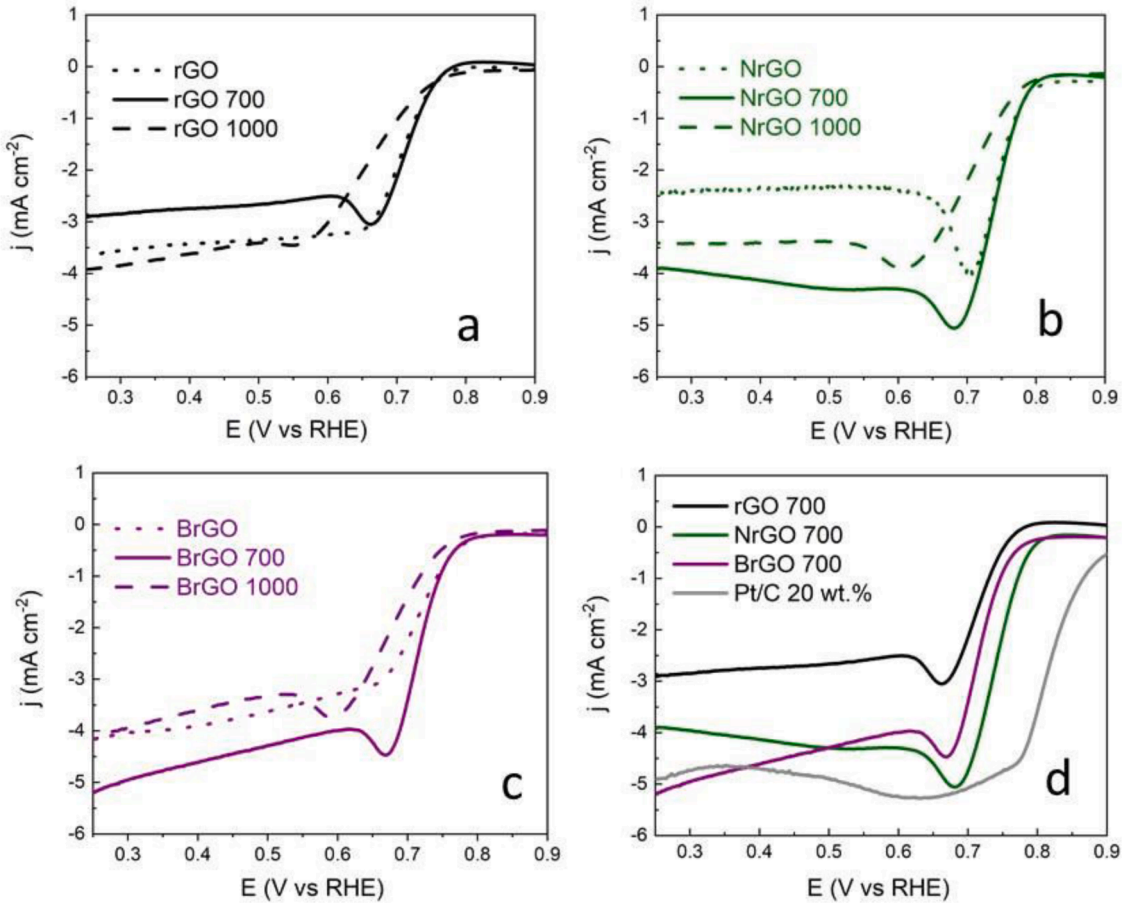

Fig. 1. LSV curves in O_2-saturated 1 M KOH electrolyte and a rotation speed of 2500 rpm for (a) rGO, (b) NrGO and (c) BrGO aerogels series: untreated (dotted line), treated at 700 °C (solid line) and treated at 1000 °C (dashed line). (d) comparison of the LSV curves for the aerogels treated a 700 °C.

Table 1
Onset potential (E_{onset}), kinetic current density (j_k), number of electrons transferred (n) and electron transfer rate (k) for ORR using the prepared graphene aerogels as electrocatalysts.

Sample	LSV curves		Koutecky-Levich analysis	
	E_{onset} (V vs RHE)	j_L *at 2500 rpm* (mA cm^{-2})	*N* (at 0.376 V vs RHE)	*K* (cm s^{-1}) x10^{-2}
rGO	0.758	3.66	2.08	2.21
rGO 700	0.758	2.86	2.80	2.98
rGO 1000	0.736	3.91	2.94	3.26
NrGO	0.799	2.41	2.94	1.15
NrGO 700	0.799	3.89	2.85	5.39
NrGO 1000	0.762	3.41	2.64	3.17
BrGO	0.767	4.16	3.85	1.95
BrGO 700	0.759	5.19	3.83	3.10
BrGO 1000	0.747	4.16	3.08	2.77

in NrGO 1000 was shifted to lower values (0.762 V vs RHE, Fig. 1b). For the three series of samples, a lower onset potential was clearly evidenced when the thermal reduction temperature was set to 1000 °C. The highest limiting currents (j_L) were obtained for the boron containing samples (Fig. 1c), specifically, for BrGO 700 (3.57 mA cm^{-2}, Table 1). In contrast, the lowest current was registered for unfunctionalized aerogels (Fig. 1a, Table 1). It was also observed that, in the case of N- and B-functionalized samples, those treated at 700 °C exhibited higher limiting currents (Fig. 1b and c). In contrast, for non-functionalized aerogel, the higher values were obtained for rGO and rGO 1000 samples (Fig. 1a). The LSV curves for the different materials was compared in Fig. 1**c** together with the 20 wt.% Pt/C benchmark ORR catalyst. The onset potential for NrGO 700 and BrGO 700 was clearly shifted to higher potentials as compared with rGO 700 but compared with Pt/C catalyst, the onset potentials of the graphene aerogels were 100–140 mV above. However, the performance of functionalized aerogels is still acceptable where the exploration of metal-free electrocatalyst is crucial for future environmental remediation. To evaluate the ORR kinetics, the LSV curves at different rotation speeds (Fig. S1) were analysed by using the Koutecky–Levich (K-L) equations (Eqs. (1)–((3). The diffusion-limited current, j_D and the kinetic current, j_K, were obtained from the slope and the intercept respectively of the Koutecky-Levich plots (j^{-1} vs $\omega^{-1/2}$) (Fig. S2). The number or transferred electrons (n) was obtained from the slope of the Koutecky-Levich plot and displayed in Table 1. The highest values of n (i.e., the more efficient is the reaction) were obtained for the boron containing samples. These values were close to 4 for the pristine and 700 °C treated sample at 0.376 V vs. RHE, i.e., close to the theoretical value for direct, 4-electron reduction of O_2 to water. The electron transfer rate constant (k) was obtained from Eq. (4) and is shown in Table 1. According to these results, the electrons were transferred faster to the oxygen molecule when using rGO 1000, BrGO 700 and NrGO 700 cathodes.

From the combined results in Table 1, the first conclusion is a clear enhancement of electrocatalytic activity through the incorporation of boron-based functional groups. Hence, BrGO series presented the highest number of transferred electrons and increased limiting current densities. The second conclusion is that the inclusion of nitrogen is also beneficial to obtain higher onset potentials. It must be considered that, even for N or B functionalized aerogels, the thermal treatment at 1000 °C decreases the number of transferred electrons. It can be therefore concluded that thermal reduction at high temperatures decreased substantially the electrocatalytic activity for all the aerogels. This was also observed for the electron transfer rate constants (k), where higher values are generally obtained for the 700 °C treated samples. This results, together with the down-shift of the ORR onset potentials, led us to dismiss the heteroatom-containing samples treated at 1000 °C. The aerogels treated at 700 °C were therefore selected for the subsequent studies, as they exhibited a better compromise between electrical conductivity (the highest heat treatment temperature, the better) and electrocatalytic activity (the lowest heat treatment temperature, the better).

3.2. Physicochemical characterization of pristine and thermally treated (700°C) graphene aerogels

Fig. 2a shows that the N_2 adsorption/desorption isotherms of the graphene aerogels belonged to type II according to the IUPAC classification, characteristic of multilayer adsorption onto essentially non-porous solids. The isotherms also showed a distinct high-relative-pressure hysteresis, typical of irregularly shaped mesopores. rGO 700 and BrGO 700 (especially the latter) exhibited low-pressure hysteresis ($P/P_0 < 0.4$). This feature likely appears due to a flexible transition in the labile matrix of graphene aerogels upon gas uptake as well as an irreversible trapping of the adsorptive [27,28]. The total pore volume was the same for rGO 700 and BrGO 700 while it was somewhat lower for NrGO 700. The BET specific surface area of rGO 700 and NrGO 700 had similar values while it was approximately half for BrGO 700 (~240 vs 104 m^2 g^{-1}, Fig. 2a). In this sense, higher surface areas had demonstrated a beneficial effect on ORR catalytic performance [13]. Fig. 2b displays a 2D-NLDFT pore size distribution, revealing that the mesopores accounted for most of the pore volume for the three aerogels. The mesopore distribution was narrower for NrGO 700 and rGO 700 (mesopore volume mostly restricted to pores up to 5 nm) while BrGO 700 featured a wide and continuous distribution of mesopores in the whole validity range of the 2D-NLDFT method, i.e., up to 30 nm. It has been previously demonstrated that the presence of a wide mesopore distribution (ranging from 5 to 25 nm) in rGO aerogels maximizes the diffusion of molecules towards the active sites in the 2D graphene structure, improving their electrochemical performance when used as Na-O_2 battery cathodes [10].

The graphene aerogels were also analyzed by EA and XPS to study their chemical composition (Table 2) before and after the treatment at 700 °C. Samples presented sulfur, nitrogen or manganese-containing residues (0.1–0.9 wt.%), probably coming from remnants of reagents used in the synthesis of GO, such as sulfuric acid, sodium nitrate and potassium permanganate, respectively [29]. The content of oxygen detected by either EA or XPS decreased to half in rGO and NrGO aerogels when treated at 700 °C. Hence, the oxygen containing functionalities in GO are generally released as CO and CO_2 by thermal treatment in inert atmosphere for temperatures above 350 °C [30]. In the case of BrGO aerogel, the content of oxygen did not decrease with the thermal treatment in BrGO 700. It can be ascribed to the formation of boron oxides on the surface of the carbon, which are not covalently-linked with carbon but adsorbed at the carbon surface as polynuclear borates [24,25]. On the other hand, the use of urea as functionalizing agent introduced high amount of nitrogen in the structure of the NrGO 700 aerogel: 5.8 wt.% in bulk (EA, Table 2) and 4 wt.% in surface (XPS, Table 2) analysis. The degree of functionalization in BrGO 700 was much lower than in the NrGO 700 sample (1.5 wt.% of surface boron by XPS analysis, Table 2) and this must be considered when evaluating the performance of the aerogels as Na-O_2 battery cathodes. However, a high heteroatom content does not always involve a better electrocatalytic activity, and other factors, such as the chemical state of oxygen, nitrogen and boron atoms, are also crucial [31].

The chemical state of the different heteroatoms was therefore studied by deconvolution of their high-resolution XPS core level spectra. The binding energies and relative weight percentages were listed in Table 3 and a scheme of the tentative chemistry evolution of the studied materials was proposed in Fig. S4. The study of the oxygen functionalities attached to the carbon atoms in the graphene sheets by analysis of the O 1 s XPS spectrum would be quite challenging. Thus, C—O and B-O bonds will present similar binding energies (BE) leading to signal overlapping [32]. Instead, the C 1 s region (280–295 eV) was used to study the chemical state of the C—O like functionalities. The spectrum was

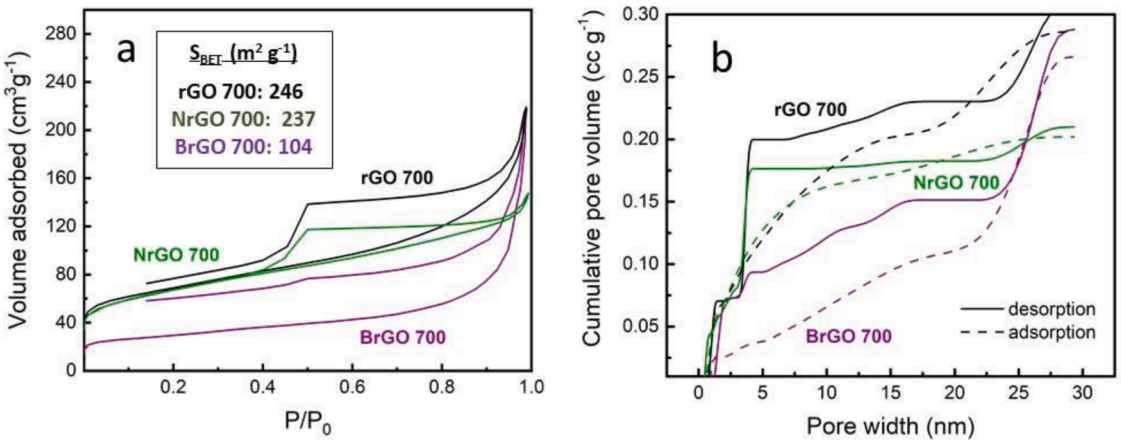

Fig. 2. (a) N_2 adsorption-desorption isotherms at −196 °C and (b) cumulative pore volumes for rGO 700, BrGO 700, and NrGO 700 aerogels.

Table 2
Bulk composition measured by EA and surface composition obtained from XPS for the graphene aerogels before and after the treatment at 700 °C.

	EA (wt.%)					XPS (wt.%)					
	C	O	N	S	H	C	O	N	S	B	Mn
rGO	78.9	18.9	1.3	0.3	1.0	85.2	14.1	0.4	0.3	–	–
NrGO	75.6	15.0	6.8	0.4	1.4	83.7	10.7	4.7	–	–	0.9
BrGO	75.0	16.6	0.8	0.3	1.1	83.0	16.0	–	–	1.0	–
rGO 700	90.2	8.0	0.7	–	1.0	93.2	6.8	–	–	–	–
NrGO 700	82.6	6.7	5.8	0.2	1.0	90.2	4.8	4.1	–	–	0.9
BrGO 700	82.1	16.2	0.4	0.1	0.6	88.0	10.4	–	–	1.6	–

Table 3
Binding energies and surface compositions obtained by deconvolution of C 1 s, N 1 s and B 1 s XPS spectra.

				XPS (wt.%)					
Spectrum	Group	notation	B.E (eV)	rGO	NrGO	BrGO	rGO 700	NrGO 700	BrGO 700
C_{1s}	graphitic C	C1	~284.5	75.8	74.3	70.8	84.8	81.5	79.9
	C sp^3, C—O, C—N	C2	~286	11.3	14.4	13.2	9.0	8.7	12.2
	C = O, C = N	C3	~287	4.2	4.2	7.3	1.1	2.7	1.5
	O-C = O	C4	~288	4.9	3.9	4.9	2.4	3.0	3.2
	π→ π*	C5	~291	3.8	3.2	3.8	2.7	4.1	3.2
N_{1s}	sp^2 N	N1	~398	–	34.1	–	–	47.3	–
	sp^3 N	N2	~399	–	45.3	–	–	26.2	–
	N quaternary	N3	~401	–	12.4	–	–	16.9	–
	N(sp^2)—O, N_2O	N4	~403	–	5	–	–	6.4	–
	N-O_X, π→ π*(sp^2 N)	N5	~405	–	3.2	–	–	3.2	–
B_{1s}	BC_2O	B1	~190	–	–	–	–	–	21.5
	BCO_2	B2	~192	–	–	33.3	–	–	69.5
	BO_3	B3	~193	–	–	69.5	–	–	9.0

deconvoluted into five components (Fig. S3 and Table 3); graphitic carbon band with maximum at BE ~284.5 eV (C1); carbon singly bonded to epoxy, hydroxyl or amide groups centered at ~286 eV (C2); doubly bonded carbon in carbonyl or imine groups at ~287 eV (C3); carbon in carboxyl groups at ~288 eV (C4) and π→π* satellite of the graphitic signal at ~291 eV (C5). Groups implying carbon singly-bonded to N or O (C2) were the dominant functionality for all the prepared graphene aerogels. BrGO presented a significant proportion of C = O type bonding (C3, 7.3 wt.% vs 4.2 wt.% in NrGO and rGO). The amount of carbonyl groups in the boron-containing aerogel decreased substantially after the thermal treatment, where the weight ratio in BrGO 700 is similar to the other heat-treated aerogels (~1.1–2.7 wt.%). It is concluded that, regardless of the relative amount of C = O functionalities, they were all released as CO or CO_2 during the thermal treatment at 700 °C [33]. In fact, the amount of oxygen-containing groups decreased for all the samples after thermal treatment by increment of the graphitic component (C1). However, BrGO 700 still presented a notable contribution of C—O functionalities (C2). The phenolic groups present on the edges of the graphene sheets could react with the polynuclear borates deposited on the surface of the aerogel which will prevent the C—O groups from volatilization during the thermal treatment (Fig. S5). This did not happen in NrGO 700 aerogel as nitrogen oxides are generally gaseous and will evolve from the graphene surface under thermal treatment. The contribution of the π→ π* component (C5) was higher for NrGO 700 (4.1 wt.%) than that in the other heat-treated aerogels (2.7–3.2 wt.%). This could be explained by a higher electron density in the π-cloud of when nitrogen atoms are introduced into the aromatic carbon lattice. As well, a larger contribution of C3 in NrGO 700 suggested the formation of imines or a possible introduction of nitrogen atoms into the graphene lattice, substituting carbon atoms. No component for C-B at ~284 eV was detected in the C 1 s core level band.

The N 1 s region (396–407 eV) was deconvoluted into five peaks (Fig. 3 and Table 3), sp^2 nitrogen in imine or pyridine form at ~398 eV (N1); sp^3 nitrogen in amine, amide, pyrrole or pyridone form ~399 eV (N2); quaternary N either in ammonium or substitutional in the graphene carbon network or as pyridinium or in the basal planes at ~401

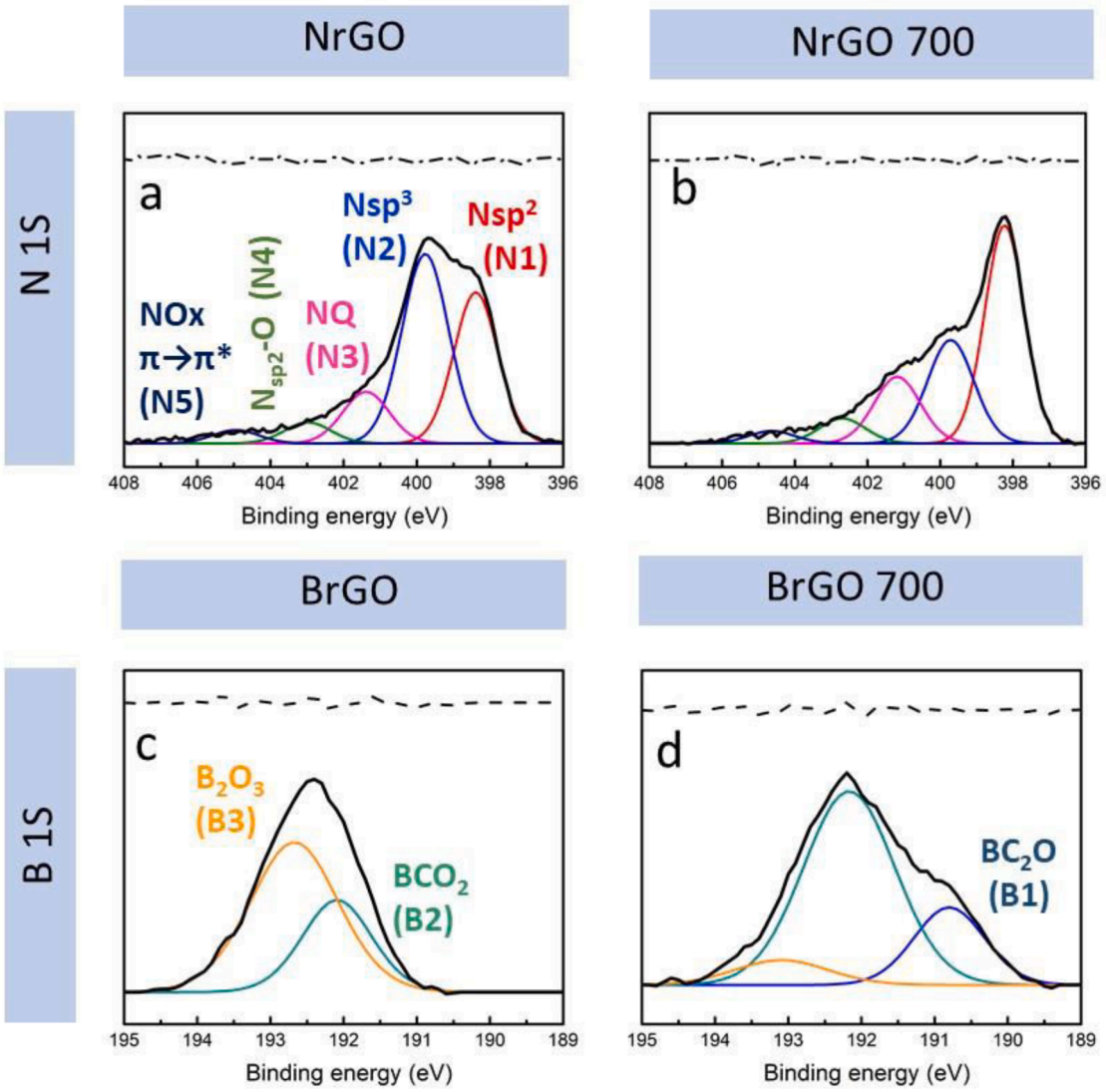

Fig. 3. XPS spectra and deconvolutions for the N 1 s region in (a) NrGO and (b) NrGO 700 and for the B 1 s region in (c) BrGO and (d) BrGO 700 aerogels.

eV (N3); nitroso or pyridine—N-oxides ~403 eV (N4) and π→π* satellite corresponding to sp^2 N and/or NOx at ~405 eV (N5). Thermally unstable groups, such as amines and amides (N2), transformed into more stable functionalities after the treatment at 700 °C, leading to a preponderance of substitutional nitrogen in the graphene network, either in the edges (N1) of the sheets or in the basal plane (N3). The most probable scenario is the transformation of pyrrolic nitrogen (5 atom ring, N2) into pyridinic like functionalities (6 atom ring, N1). A slight increase in the quaternary nitrogen (N3) and N—O oxides (N4) was also verified. The B 1 s region (188–196 eV region) was satisfactory fitted by means of three peaks (Fig. 3 and Table 3); boron covalently bonded to two carbon atoms at ~190 eV (B1) or one carbon atom at ~192 eV (B2) on the edges of the carbon lattice; and boron in oxides which are not covalently liked to carbon at ~193 eV (B3). The untreated BrGO sample presented mostly boron oxides not linked to the carbon lattice but deposited on its surface (B3). The treatment of the aerogel up to 700 °C led to the formation of covalent C-B bonding (BCO_2, B2) or even the introduction of substitutional boron atom in BC_2O like groups (B1) at the edge of the graphene sheets. Even though boron was not detected in a full substitutional environment (BC_3 groups) in any of the samples, the introduction of BC_2O into the carbon lattice could modify the electronic structure of graphene. Unlike C 1 s spectra, B 1 s core level shows the presence of B-C bonds. It can be ascribed to the high relative contribution of the B-C moiety to the whole B 1 s signal as compared to that in C 1 s intensity. Indeed, boron appeared in low proportion (1–2 at.%) while carbon is the majoritarian element (86–90 at.%). Therefore, the signal coming from boron could be a maximum of 3–6 at.% of the total C1s signal, and that is assuming that all boron is bonded to carbon (in the form BC_3) while any other possibility (BC_2O or BCO_2) will lead to even lower proportions of C-B in the C 1 s signal.

3.3. SEM imaging and cycling performance of the graphene-based cathodes

As described in the experimental section, the graphene aerogel powders were deposited onto a commercial GDL to prepare battery cathodes. The SEM images of the clean GDL support showed nanometric spherical particles, typical of carbon, the black product used in the microporous layer (Fig. 4a). In contrast, the deposition of crumpled graphene sheets on the top of the GDL was verified for the prepared cathodes (Fig. 4b–d). The deposition of the graphene sheets in the N- and B- functionalized samples seemed very homogeneous when observed by SEM at lower magnification (Fig. S6c and S6d). However, rGO 700 clearly presented more heterogeneous and less uniform coating (Fig. S6b) and detached when manipulating the electrode (Fig. S7). It is important to note that the size of graphene objects observed by SEM

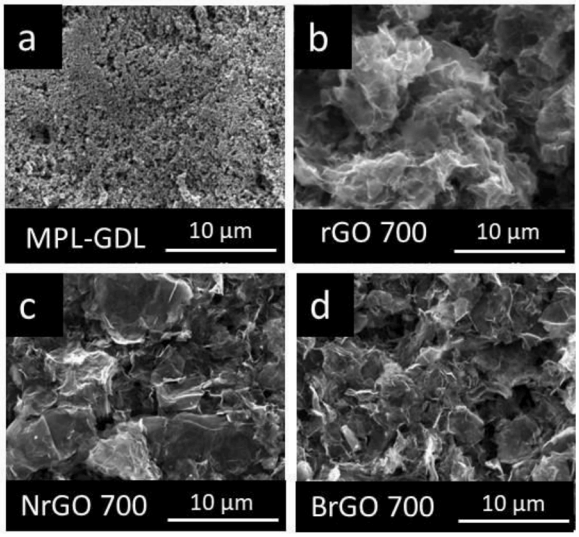

Fig. 4. × 10,000 SEM images of (a) the commercial GDL used as support from the microporous layer side and the different GDLs coated with the graphene aerogels (b) rGO 700, (c) NrGO 700, and (d) BrGO 700.

imaging was different from one aerogel to another. Hence, rGO 700 and BrGO 700 aerogels yielded agglomerations of smaller objects ~2–5 µm in lateral size where NrGO 700 presented larger particles about 10 µm, respectively. Such difference in size could be ascribed to the sonication time needed for the preparation of stable inks for each aerogel to be coated into the GDL support. It has been reported that differences in sheet size cause variations of the electrocatalytic activity due to an increase of reactive defects in the graphene structure, which are mainly located at the edge of the layers. However, such performance variability is verified for differences in size as significant as one order of magnitude [34] and not for differences of few micrometers, as occurring in this study after sonication. SEM imaging is a good tool to study the size of particles but not to measure the size of nanometric graphene sheets, as they are usually stack with each other. To verify the lateral size of the graphene sheets after sonication, the crystallite size was estimated by the Tuinstra–Koenig correlation using Raman spectroscopy (Fig. S8). The crystallite size calculated from I_D/I_G relation was ~2 µm for all the studied aerogels. As well, the similar shape, intensity and shift of 2D band indicates that the number of layers in graphene also remains constant. It can be concluded that the differences in the electrocatalytic or cathode performance of the graphene did not arise from the differences on the sheet size. Hence, the longer sonication time required to disperse NrGO 700 aerogel (4 vs 2 h for other aerogels), seemed to produce the agglomeration of the graphene sheets into bigger particles and slightly lower graphene or graphene/heteroatom catalyst loading. Thus, the average graphene loadings deposited over the GDL were: 1.50 mg cm^{-2} for rGO 700, 1.45 mg cm^{-2} for BrGO 700, and 0.74 mg cm^{-2} for the NrGO 700. Even though the catalyst loading for NrGO 700 is half than other aerogels, the amount of nitrogen is twice the amount of boron in BrGO 700 (Table 2). Therefore, a fair comparison of the electrochemical performance based on the electroactive active centres (heteroatoms) was still possible. For electrode manufacture, it is important to consider that rGO 700 and BrGO 700 formed stable inks, homogeneous and mechanically stable coatings with high material loading. These characteristics are not simultaneously met by the aerogel functionalized with nitrogen.

The cycling performance of the GDL-supported rGO 700, NrGO 700 and BrGO 700 cathodes was studied by galvanostatic charge/discharge at 0.2 mA cm^{-2} using 0.1 M NaOTf in DME electrolyte and limiting the cycling capacity to 0.5 mAh cm^{-2}. Both rGO 700 and BrGO 700 delivered 70 cycles while the life of the NrGO 700 cathode was limited to 48 cycles (Fig. 5a–c). The charging stability of BrGO was much better than that of the other graphene aerogels where the efficiency of the battery reached 100% only after 9 cycles. In contrast, rGO 700 and NrGO 700 needed 28–45 cycles to reach such efficiency. The cycling overpotential (ORR + OER overpotential) of the cathodes was monitored at 0.2 mAh cm^{-2} and the functionalized aerogels presented a decreased value compared with rGO 700 (Fig. 5d). BrGO 700 yielded the lowest overpotential, which stabilized below 150 mV from the ~20 to 60th cycle. It can be concluded that the functionalization of graphene aerogel with C-B covalent bonding, either as oxide chains linked to the carbon edges (BCO_2) or substituting the carbon atom (BC_2O) also at edges, provided the material with enhanced electrocatalytic activity towards both ORR and OER reactions. This resulted in a longer cycle life, higher efficiency and lower discharge/cycling overpotentials in the Na-O_2 battery.

3.4. Assessment of the discharge and charge performance of the graphene-based cathodes

To understand the enhanced cyclability and efficiency of BrGO 700 aerogel compared with its non-functionalized and N-functionalized counterparts, the full discharge (ORR) and charge (OER) performance was studied. The discharge profiles for the different samples were displayed in Fig. 6a. The undoped aerogel (rGO 700) presented larger discharge capacity (4.63 mAh cm^{-2}) than NrGO 700 (4.07 mAh cm^{-2}) and BrGO 700 (4.27 mAh cm^{-2}) cathodes. However, the obtained values were not very different, and it can be considered that the three cathodes presented similar discharge capacity. The discharge overpotential, which is the difference between (1) the standard reduction potential of O_2 gas to superoxide (2.27 V, dotted line in abscissa in Fig. 6a) and (2) the potential at which the reaction actually occurs (plateau in the discharge curve), is also an important parameter in the electrochemical performance of a cathode. High overpotential values are detrimental as they are related to kinetic limitations and, consequently, a decreased power density in the battery. NrGO 700 and rGO 700 presented similar discharge overpotential (230 mV) while BrGO 700 yields favored ORR kinetics due to a lower overpotential (195 mV). The charging performance (OER) was also studied by full charging/discharging the different cathodes for 1 cycle (Fig. 6b). Similar to discharge, BrGO 700 yielded the lowest charge overpotential compared with the other cathodes (see inlet in Fig. 6b). Thus, the cycle hysteresis (voltage difference between discharge and charge plateaus) at 1 mAh cm^{-2} was ~ 320, ~333 and 279 mV for rGO 700, NrGO 700 and BrGO 700, respectively. This suggested a bifunctional electrocatalytic activity of BrGO towards both ORR and OER reactions. rGO 700 was unable to complete the charge and, for capacities above 3 mAh cm^{-2}, a noisy voltage profile was evidenced. This phenomenon is usually caused by transient short circuits, and in the particular case of this cell, it was probably caused by the poor mechanical stability of the rGO 700 coating (Figs. S6 and S7). The graphene could detach from the GDL cathode during battery operation and get in contact with the sodium anode trough the edges of the Celgard separator. Besides the charge instability in rGO 700, the functionalization of the graphene aerogel also affected the coulombic efficiency, where the rGO 700 cathode presented a coulombic efficiency of 79%, while BrGO 700 and NrGO had higher efficiencies (88% and 86%, respectively).

The fully discharged and/or charged cathodes in Fig. 6 were analyzed by SEM imaging (Fig. 7) and Raman/NMR spectroscopies (Fig. 8). The fully discharged cathodes displayed cube like discharge products, which is a typical morphology of sodium superoxide (NaO_2) crystals. It can be noticed that the functionalized cathodes displayed more densely distributed discharge products (Fig. 7b and 7c), implying that both boron and nitrogen doping increased the active area where ORR takes place. The cubes in BrGO 700 and rGO 700 presented similar size ~10 µm (Fig. 7a and 7c), while those in NrGO 700 were larger (~20 µm, Fig. 7b). After charging, both rGO 700 and BrGO 700 cathodes (Fig. 7d and 7f) showed smooth surfaces similar to pristine cathodes in Fig. 4, indicating that the discharge products were effectively eliminated

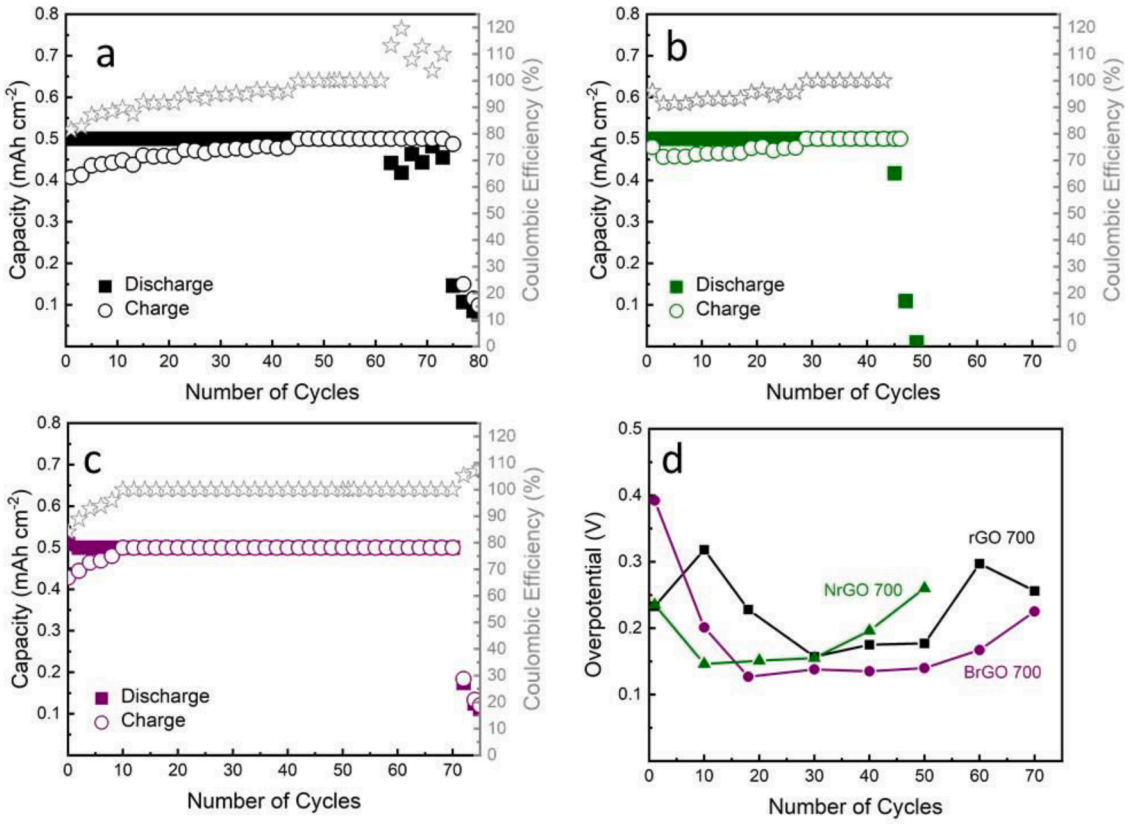

Fig. 5. Evolution of discharge capacity (left axis, points denoted as filled symbols), charge capacity (left axis, points denoted as open symbols) and columbic efficiency (right, gray axis, gray stars) for (a) rGO 700, (b) NrGO 700 and (c) BrGO 700. (d) comparison of the cycling overpotential as function of the number of cycles for the three cathode materials.

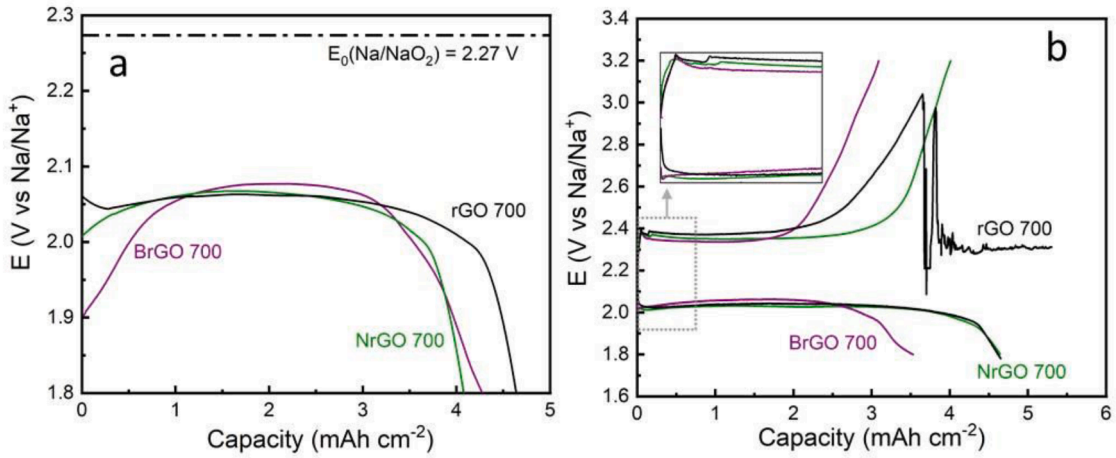

Fig. 6. (a) Galvanostatic full discharge and (b) galvanostatic full discharge/charge profiles for doped and undoped cathodes 0.2 mA cm^{-2} using 0.1 M NaOTf in DME and inset for the 0 to 0.5 mAh cm^{-2} region.

once the full charge was completed. However, NrGO 700 presented a clear passivation of film-like or cuboid morphologies (Fig. 7e). This indicated the formation of discharge products which could not be dissolved back into the electrolyte and, consequently, oxidized to O_2 gas during charge. It has been demonstrated that cathodes with high surface energy and enhanced oxygen binding affinity promote the nucleation of the discharge products directly on the cathode surface [35]. That situation could well be in place when boron is introduced as substitutional BC_2O groups in the carbon lattice of the graphene aerogels. Specifically, boron has one less valence electron than carbon, and will therefore induce local positive charges in the lattice (Fig. S9). The interaction of oxygen species (either O_2 gas or already reduced species) with such positive charges will promote the direct nucleation and growth of the NaO_2 cubes on the surface of the cathode (surface mediated mechanism), leading to lower particle size. The situation for nitrogen atom is exactly the opposite, where one more valence electron relative to carbon will increase the local electron density (Fig. S9). This will repel the O_2^- species (reduced in the cathode) towards the electrolyte phase, promoting the nucleation and growth of the NaO_2 cubes on the electrolyte bulk to further precipitate onto the cathode surface (the solution

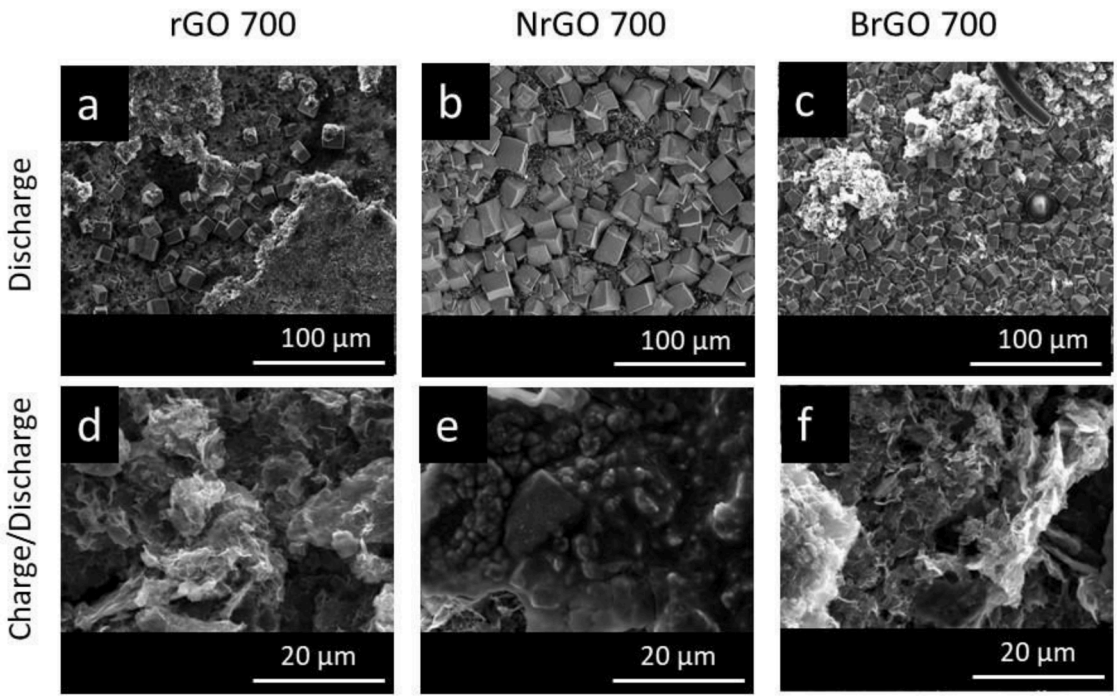

Fig. 7. SEM images of the graphene aerogel cathodes after full discharge (a) rGO 700, (b) NrGO 700, and BrGO 700 and after full charge/discharge (a) rGO 700, (b) NrGO 700, and BrGO 700 at 0.2 mA cm^{-2} using 0.1 M NaOTf in DME.

mediated mechanism). The nucleation and growth of the superoxide product in the electrolyte phase is also known to promote the formation of hydroperoxyl and singlet oxygen ($^1O_2$), which is known to be the main driver for parasitic chemistry in metal-air batteries [36,37]. This could explain the formation of bigger cubes on the surface of NrGO 700 during charge (Fig. 7b) and the presence of insoluble parasitic products after charging (Fig. 7e). This hypothesis is consequent with computational predictions where the adsorption of NaO_2 molecules on the surface of boron doped graphene occurs via a dissociative mechanism of O_2 molecules, which are strongly adsorbed on the surface of the cathode. In contrast, the calculations for pristine and nitrogen doped graphene pointed to the adsorption of an already dissociated molecule as the interaction with O_2 is not so strong [38].

The existence of NaO_2 as the main discharge product in all the discharged cathodes was confirmed by Raman spectroscopy (Fig. 8a). All the discharged samples presented a sharp peak at 1156 cm^{-1} characteristic of NaO_2, together with the archetypal D and G bands of graphenic/graphitic materials at 1355 and 1597 cm^{-1}, respectively. The NaO_2 peak completely disappeared upon charging, which confirmed that NaO_2 was completely oxidated after charge. As well, it also indicated that any deposits left on the surface of the cathode were parasitic products, but not NaO_2. Importantly, these observations were valid for all the three materials, including rGO 700 where the galvanostatic charge curve become rippled above 3 V vs Na/Na^+ (Fig. 6b). Solid state ^{23}Na NMR was conducted for the discharged cathodes (Fig. 8b). A well-defined signal centered at around −26 ppm was observed in the samples. This signal was observed before in the postmortem characterization of Na-O_2 batteries and was assigned to the formation of NaO_2 on the discharged cathodes [10,39–43]. An additional sharp peak at −15 ppm with a wide shoulder extended up to ~10 ppm was also observed. This shift was previously ascribed to the formation of carbonates [40,44,45]. Even though all the cathodes developed parasitic products after full discharge, their abundance appeared to be much higher in NrGO 700 (Fig. 8b). This is consistent with SEM imaging in Fig. 7e, where the presence of undissolved amorphous products after charging was much more evident for NrGO 700. In contrast, the cathode with the lowest ratio of parasitic products was rGO 700. The existence of a larger proportion of carbonates in NrGO 700 suggested an independent secondary phenomenon that was related to the surface chemistry/structure of the cathode material. It is known that the superoxide is a strong oxidizing agent [46], which could oxidize carbon atoms at the defects of the graphene material to give carbonates ($2NaO_2 + C \rightarrow Na_2CO_3 + 1/2\ O_2$). It seems that the presence of nitrogen in the aerogel structure promotes the oxidation of the carbon to form those parasitic products. After full charge, the NaO_2 peak at −26 ppm vanished for NrGO 700 and BrGO 700, but it was still observed to some extent for rGO 700 (Fig. 8b). This can be readily explained by the uncomplete charge of the battery assembled with rGO 700 due to the occurrence of internal short circuits (Fig. 6b). On the other hand, all the graphene cathodes exhibited on their surface insoluble parasitic products that were not oxidized during the charge cycle (Fig. 8b). It is important to note that, in contrast to solid NMR, discharge products other than NaO_2 were not observed by Raman spectroscopy in Fig. 8a. This could be related to the detection limit of the different characterization techniques where the detection of parasitic products is not always straightforward [47]. In this sense, the laser beam in Raman spectroscopy could decompose the sodium carbonate by overheating the product and releasing as CO_2. As well, the sampling depth in Raman is around 150 µm in contrast to solid NMR with is much more sensitive to the whole sample bulk. On the other hand, the soluble discharge products existing after discharge were analyzed by soaking the three different electrodes in DMSO-d^6 for 15 h and analyzing the extract by liquid ^1H NMR. No information could be obtained from ^{13}C NMR due to the very low concentration of the secondary products in the extracted solution. Both sodium formate and acetate were identified in the ^1H NMR spectra from the peaks at 8.52 and 1.6 ppm (Fig. S10), respectively [40]. These products are generally produced by the degradation of the electrolyte [48] through oxidative nucleophilic attack of NaO_2. In the case of NrGO 700 an extra impurity was observed which was not possible to identify due to its extremely low concentration. The integration of the peaks corresponding to the different products enabled the relative quantification of each product, and their weight percentages were displayed in Fig. 8c. Compared with the N- and B- functionalized samples, rGO 700 exhibited the largest proportion of parasitic products, in form of formates and acetates. From solid state and

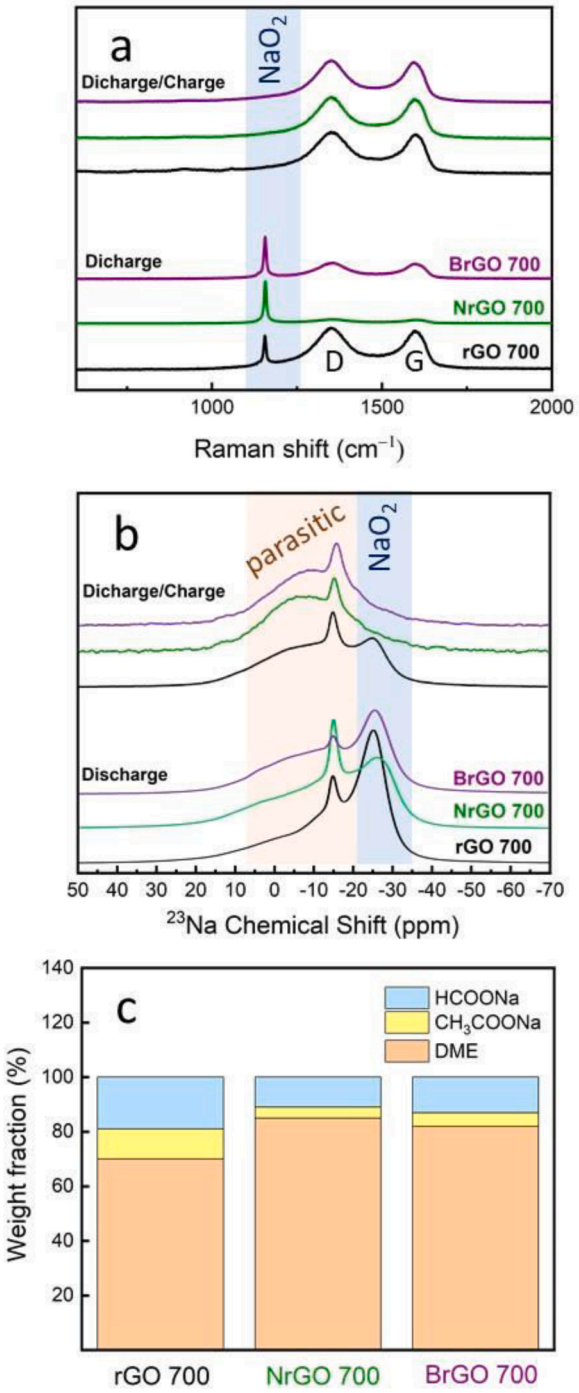

Fig. 8. (a) Raman spectroscopy of cathodes upon full discharge and subsequent full charge. (b) ^{23}Na solid state NMR spectra of the discharge and discharge/charge cathodes. (c) ^{1}H liquid NMR analysis of the solution obtained after soaking the discharge cathodes in DMSO-d^{6} solvent (complete spectra in Fig. S10).

liquid NMR, it can be concluded that BrGO was the sample presenting the lowest overall ratio of parasitic products, either soluble or insoluble.

The results reported in this study are in line with the DFT work reported by Benti et al. [19]., where they predicted that both single- and double-boron-atom-doped graphene exhibited too low discharge/charge overpotentials, indicating high catalytic activities towards both the ORR and OER processes compared to other doped graphene samples. Unlike one- and two-nitrogen-doped graphene which essentially did not exhibit an enhanced performance. Moreover, apart from boron presenting better catalytic activity, heteroatom doped could be also use as a strategy for minimizing the parasitic chemistry in metal-air batteries which leads to poor cycling performance.

4. Conclusions

Hydrothermally derived graphene oxide aerogels were functionalized with nitrogen and boron and reduced by thermal treatment to different temperatures under inert atmosphere. An increased performance for the air cathode with boron-containing functional groups was observed. This resulted in a superiorcharge capacity by at least 25%, when compared to non-doped cathodes, while simultaneously enabling up to 70 cycles at a relatively high current density (0.1 mA cm^{-2}) using a capacity cut-off of 0.5 mAh cm^{-2}. By contrast, functionalization with nitrogen triggered the formation of solid parasitic products which passivated the cathode surface during cycling and increased the cell overpotential and decreased the cycle life. The introduction of boron in the graphene lattice in different covalently bonded configurations, i.e., oxide chains linked to carbon edges (BCO_2) or having double bonding to carbon (BC_2O) also at edges, provided the material with enhanced electrocatalytic activity towards ORR/OER reactions. This resulted in a longer cycle life, higher efficiency and lower discharge/cycling overpotentials in corresponding Na-O_2 battery. Such an enhanced performance could be also related to the generation of a lower number of parasitic products in the boron-functionalized sample. The lower electronegative character of boron compared with carbon was thought to generate positive charges in the graphene lattice, resulting in enhanced adsorption of oxygen species and, consequently, higher electroactivity of the material.

CRediT authorship contribution statement

M. Enterría: Conceptualization, Formal analysis, Methodology, Data curation, Validation, Writing – original draft, Visualization. **R. Mysyk:** Investigation, Data curation, Writing – review & editing, Visualization. **L. Medinilla:** Investigation, Data curation, Methodology, Writing – review & editing. **S. Villar-Rodil:** Investigation, Formal analysis, Writing – review & editing. **J.I. Paredes:** Formal analysis, Writing – review & editing. **I. Rincón:** Investigation, Writing – review & editing. **F.J. Fernández-Carretero:** Formal analysis, Methodology, Data curation, Validation, Writing – review & editing. **K. Gómez:** Investigation, Formal analysis, Writing – review & editing. **J.M. López del Amo:** Investigation, Formal analysis, Writing – review & editing. **N. Ortiz-Vitoriano:** Conceptualization, Formal analysis, Methodology, Resources, Supervision, Project administration, Funding acquisition, Writing – review & editing.

Declaration of Competing Interest

The authors declare the following financial interests/personal relationships which may be considered as potential competing interests

Data availability

Data will be made available on request.

Acknowledgements

This work was funded by the European Union (Graphene Flagship-Core 3, Grant number 881603) and the Basque Country Government (CIC energiGUNE'20 of the ELKARTEK program, N° Exp. KK-2020/0078). J.I.P. and S.V.-R. acknowledge funding by the Spanish Ministerio de Ciencia e Innovación and Agencia Estatal de Investigación (MCIN/AEI/ 10.13039/501100011033) as well as the European Regional Development Fund (ERDF, A way of making Europe) through

grant PID2021-125246OB-I00, and by Plan de Ciencia, Tecnología e Innovación (PCTI) 2018-2022 del Principado de Asturias and the ERDF through grant IDI/2021/000037. N. Ortiz-Vitoriano thanks Ramon y Cajal grant (RYC-2020-030104-I) funded by MCIN/AEI/10.13039/501100011033 and by FSE invest in your future.

Supplementary materials

Supplementary material associated with this article can be found, in the online version, at doi:10.1016/j.electacta.2023.142056.

References

[1] U. Salahuddin, H. Ejaz, N. Iqbal, Grid to wheel energy efficiency analysis of battery- and fuel cell–powered vehicles, Int. J. Energy Res. 42 (2018) 2021–2028, https://doi.org/10.1002/er.3994.
[2] W. Tahil, M.I. Research, The Trouble with Lithium; Implications of Future PHEV Production for Lithium Demand, Meridian International Research, 2007. http://www.meridian-int-res.com/Projects/Lithium_Problem_2.pdf.
[3] H. Yadegari, Y. Li, M.N. Banis, X. Li, B. Wang, Q. Sun, R. Li, T.K. Sham, X. Cui, X. Sun, On rechargeability and reaction kinetics of sodium-air batteries, Energy Environ. Sci. 7 (2014) 3747–3757, https://doi.org/10.1039/c4ee01654h.
[4] F. Wu, Y. Xing, J. Lai, X. Zhang, Y. Ye, J. Qian, L. Li, R. Chen, Micrometer-sized RuO_2 catalysts contributing to formation of amorphous Na-deficient sodium peroxide in Na–O_2 batteries, Adv. Funct. Mater. 27 (2017), 1700632, https://doi.org/10.1002/adfm.201700632.
[5] H. Yadegari, X. Sun, Recent advances on sodium-oxygen batteries: a chemical perspective, Acc. Chem. Res. 51 (2018) 1532–1540, https://doi.org/10.1021/acs.accounts.8b00139.
[6] H. Yadegari, C.J. Franko, M.N. Banis, Q. Sun, R. Li, G.R. Goward, X. Sun, How to control the discharge products in Na-O_2 cells: direct evidence toward the role of functional groups at the air electrode surface, J. Phys. Chem. Lett. 8 (2017) 4794–4800, https://doi.org/10.1021/acs.jpclett.7b02227.
[7] X. Lin, Q. Sun, K. Doyle Davis, R. Li, X. Sun, The application of carbon materials in nonaqueous Na-O_2 batteries, Carbon Energy 1 (2019) 141–164, https://doi.org/10.1002/cey2.15.
[8] J.L. Gómez Urbano, M. Enterría, I. Monterrubio, I. Ruiz de Larramendi, D. Carriazo, N. Ortiz Vitoriano, T. Rojo, An overview of engineered graphene-based cathodes: boosting oxygen reduction and evolution reactions in lithium– and sodium–oxygen batteries, ChemSusChem 13 (2020) 1203–1225, https://doi.org/10.1002/cssc.201902972.
[9] X. Lin, J. Wang, X. Gao, S. Wang, Q. Sun, J. Luo, C. Zhao, Y. Zhao, X. Yang, C. Wang, R. Li, X. Sun, 3D printing of free-standing "O_2 breathable" air electrodes for high-capacity and long-life Na-O_2 batteries, Chem. Mater. 32 (2020) 3018–3027, https://doi.org/10.1021/acs.chemmater.9b05360.
[10] M. Enterría, C. Botas, J.L. Gómez-Urbano, B. Acebedo, J.M. López Del Amo, D. Carriazo, T. Rojo, N. Ortiz-Vitoriano, Pathways towards high performance Na-O_2 batteries: tailoring graphene aerogel cathode porosity & nanostructure, J. Mater. Chem. A 6 (2018) 20778–20787, https://doi.org/10.1039/c8ta07273f.
[11] W. Li, C. Han, K. Zhang, S. Chou, S. Dou, Strategies for boosting carbon electrocatalysts for the oxygen reduction reaction in non-aqueous metal-air battery systems, J. Mater. Chem. A 9 (2021) 6671–6693, https://doi.org/10.1039/d1ta00203a.
[12] H. Li, T.A. Ha, N. Ortiz-Vitoriano, X. Wang, J. Fang, P.C. Howlett, C. Pozo-Gonzalo, Tunable multi-doped carbon nanofiber air cathodes based on a poly(ionic liquid) for sodium oxygen batteries with diglyme/ionic liquid-based hybrid electrolytes, J. Mater. Chem. A 10 (2022) 11742–11754, https://doi.org/10.1039/d2ta01586b.
[13] J.L. Ma, X.B. Zhang, Optimized nitrogen-doped carbon with a hierarchically porous structure as a highly efficient cathode for Na-O_2 batteries, J. Mater. Chem. A 4 (2016) 10008–10013, https://doi.org/10.1039/c6ta02793h.
[14] Z. Zheng, J. Jiang, H. Guo, C. Li, K. Konstantinov, Q. Gu, J. Wang, Tuning NaO_2 formation and decomposition routes with nitrogen-doped nanofibers for low overpotential Na-O_2 batteries, Nano Energy 81 (2021), 105529, https://doi.org/10.1016/j.nanoen.2020.105529.
[15] Q. Sun, H. Yadegari, M.N. Banis, J. Liu, B. Xiao, B. Wang, S. Lawes, X. Li, R. Li, X. Sun, Self-stacked nitrogen-doped carbon nanotubes as long-life air electrode for sodium-air batteries: elucidating the evolution of discharge product morphology, Nano Energy 12 (2015) 698–708, https://doi.org/10.1016/j.nanoen.2015.01.018.
[16] C. Shu, Y. Lin, B. Zhang, S.B. Abd Hamid, D. Su, Mesoporous boron-doped onion-like carbon as long-life oxygen electrode for sodium-oxygen batteries, J. Mater. Chem. A 4 (2016) 6610–6619, https://doi.org/10.1039/c6ta00901h.
[17] J. Duan, S. Chen, M. Jaroniec, S.Z. Qiao, Heteroatom-doped graphene-based materials for energy-relevant electrocatalytic processes, ACS Catal. 5 (2015) 5207–5234, https://doi.org/10.1021/acscatal.5b00991.
[18] Y. Li, H. Yadegari, X. Li, M.N. Banis, R. Li, X. Sun, Superior catalytic activity of nitrogen-doped graphene cathodes for high energy capacity sodium-air batteries, Chem. Commun. 49 (2013) 11731–11733, https://doi.org/10.1039/c3cc46606j.
[19] N.E. Benti, G.A. Tiruye, Y.S. Mekonnen, Boron and pyridinic nitrogen-doped graphene as potential catalysts for rechargeable non-aqueous sodium-air batteries, RSC Adv. 10 (2020) 21387–21398, https://doi.org/10.1039/d0ra03126g.
[20] B. Jiang, C. Tian, L. Wang, L. Sun, C. Chen, X. Nong, Y. Qiao, H. Fu, Highly concentrated, stable nitrogen-doped graphene for supercapacitors: simultaneous doping and reduction, Appl. Surf. Sci. 258 (2012) 3438–3443, https://doi.org/10.1016/j.apsusc.2011.11.091.
[21] Y. Wang, C. Wang, Y. Wang, H. Liu, Z. Huang, Boric acid assisted reduction of graphene oxide: a promising material for sodium-ion batteries, ACS Appl. Mater. Interfaces 8 (2016) 18860–18866, https://doi.org/10.1021/acsami.6b04774.
[22] Adsorption by Powders and Porous Solids, Elsevier, 1999, https://doi.org/10.1016/b978-0-12-598920-6.x5000-3.
[23] J. Jagiello, J.P. Olivier, 2D-NLDFT adsorption models for carbon slit-shaped pores with surface energetical heterogeneity and geometrical corrugation, Carbon 55 (2013) 70–80, https://doi.org/10.1016/j.carbon.2012.12.011.
[24] T. Priamushko, E. Budiyanto, N. Eshraghi, C. Weidenthaler, J. Kahr, M. Jahn, H. Tüysüz, F. Kleitz, Incorporation of Cu/Ni in ordered mesoporous Co-based spinels to facilitate oxygen evolution and reduction reactions in alkaline media and aprotic Li−O_2 batteries, ChemSusChem 15 (2022), e202102404, https://doi.org/10.1002/cssc.202102404.
[25] J. Suntivich, H.A. Gasteiger, N. Yabuuchi, H. Nakanishi, J.B. Goodenough, Y. Shao-Horn, Design principles for oxygen-reduction activity on perovskite oxide catalysts for fuel cells and metal-air batteries, Nat. Chem. 3 (2011) 546–550, https://doi.org/10.1038/nchem.1069.
[26] T. Huang, S. Mao, G. Zhou, Z. Wen, X. Huang, S. Ci, J. Chen, Hydrothermal synthesis of vanadium nitride and modulation of its catalytic performance for oxygen reduction reaction, Nanoscale 6 (2014) 9608–9613, https://doi.org/10.1039/c4nr02646b.
[27] C. Reichenbach, D. Enke, J. Möllmer, D. Klank, M. Klauck, G. Kalies, Slow gas uptake and low pressure hysteresis on nanoporous glasses: the influence of equilibration time and particle size, Microporous Mesoporous Mater. 181 (2013) 68–73, https://doi.org/10.1016/j.micromeso.2013.07.007.
[28] M. Stojmenović, M. Vujković, L. Matović, J. Krstić, A. Dukić, V. Dodevski, S. M. Živković, S. Mentus, Complex investigation of charge storage behavior of microporous carbon synthesized by zeolite template, Microporous Mesoporous Mater. 228 (2016) 94–106, https://doi.org/10.1016/j.micromeso.2016.03.029.
[29] H. Yu, B. Zhang, C. Bulin, R. Li, R. Xing, High-efficient synthesis of graphene oxide based on improved hummers method, Sci. Rep. 6 (2016) 1–7, https://doi.org/10.1038/srep36143.
[30] R. Rocha, O. Soares, J. Figueiredo, M. Pereira, Tuning CNT properties for metal-free environmental catalytic applications, C 2 (2016) 17, https://doi.org/10.3390/c2030017.
[31] M. Enterría, J.L. Figueiredo, Nanostructured mesoporous carbons: Tuning texture and surface chemistry, Carbon 108 (2016) 79–102, https://doi.org/10.1016/j.carbon.2016.06.108.
[32] M. Enterría, M.F.R. Pereira, J.I. Martins, J.L. Figueiredo, Hydrothermal functionalization of ordered mesoporous carbons: The effect of boron on supercapacitor performance, Carbon 95 (2015) 72–83, https://doi.org/10.1016/j.carbon.2015.08.009.
[33] J.L. Figueiredo, M.F.R. Pereira, The role of surface chemistry in catalysis with carbons, Catal. Today 150 (2010) 2–7, https://doi.org/10.1016/j.cattod.2009.04.010.
[34] J. Benson, Q. Xu, P. Wang, Y. Shen, L. Sun, T. Wang, M. Li, P. Papakonstantinou, Tuning the catalytic activity of graphene nanosheets for oxygen reduction reaction via size and thickness reduction, ACS Appl. Mater. Interfaces 6 (2014) 19726–19736, https://doi.org/10.1021/am5048202.
[35] L. Lutz, D.A.D. Corte, Y. Chen, D. Batuk, L.R. Johnson, A. Abakumov, L. Yate, E. Azaceta, P.G. Bruce, J.M. Tarascon, A. Grimaud, The role of the electrode surface in Na–air batteries: insights in electrochemical product formation and chemical growth of NaO_2, Adv. Energy Mater. 8 (2018), https://doi.org/10.1002/aenm.201701581.
[36] N. Mahne, B. Schafzahl, C. Leypold, M. Leypold, S. Grumm, A. Leitgeb, G. A. Strohmeier, M. Wilkening, O. Fontaine, D. Kramer, C. Slugovc, S.M. Borisov, S. A. Freunberger, Singlet oxygen generation as a major cause for parasitic reactions during cycling of aprotic lithium-oxygen batteries, Nat. Energy 2 (2017) 1–9, https://doi.org/10.1038/nenergy.2017.36.
[37] J.M. Munuera, J.I. Paredes, M. Enterría, S. Villar-Rodil, A.G. Kelly, Y. Nalawade, J. N. Coleman, T. Rojo, N. Ortiz-Vitoriano, A. Martínez-Alonso, J.M.D. Tascón, High performance Na-O_2 batteries and printed microsupercapacitors based on water-processable, biomolecule-assisted anodic graphene, ACS Appl. Mater. Interfaces 12 (2020) 494–506, https://doi.org/10.1021/acsami.9b15509.
[38] K.A. Novčić, A.S. Dobrota, M. Petković, B. Johansson, N.V. Skorodumova, S. V. Mentus, I.A. Pašti, Theoretical analysis of doped graphene as cathode catalyst in Li-O_2 and Na-O2 batteries – the impact of the computational scheme, Electrochim. Acta 354 (2020), https://doi.org/10.1016/j.electacta.2020.136735.
[39] L. Garcia-Quintana, N. Ortiz-Vitoriano, H. Zhu, G.M. Nolis, J. Herrero-Martín, M. Echeverría, J.M. López del Amo, M. Forsyth, A.M. Bond, P.C. Howlett, C. Pozo-Gonzalo, Unveiling the impact of the cations and anions in ionic liquid/glyme hybrid electrolytes for Na–O_2 batteries, ACS Appl. Mater. Interfaces 14 (2022) 4022–4034, https://doi.org/10.1021/acsami.1c20257.
[40] T. Liu, G. Kim, M.T.L. Casford, C.P. Grey, Mechanistic Insights into the challenges of cycling a nonaqueous Na-O_2 battery, J. Phys. Chem. Lett. 7 (2016) 4841–4846, https://doi.org/10.1021/acs.jpclett.6b02267.
[41] N. Ortiz-Vitoriano, I. Monterrubio, L. Garcia-Quintana, J.M. López Del Amo, F. Chen, T. Rojo, P.C. Howlett, M. Forsyth, C. Pozo-Gonzalo, Highly homogeneous sodium superoxide growth in Na-O_2 batteries enabled by a hybrid electrolyte, ACS Energy Lett. 5 (2020) 903–909, https://doi.org/10.1021/acsenergylett.0c00081.
[42] T.R. Krawietz, D.K. Murray, J.F. Haw, Alkali metal oxides, peroxides, and superoxides: a multinuclear MAS NMR study, J. Phys. Chem. A 102 (1998) 8779–8785, https://doi.org/10.1021/jp9823190.

[43] C. Pozo-Gonzalo, Y. Zhang, N. Ortiz-Vitoriano, J. Fang, M. Enterría, M. Echeverría, J.M. López del Amo, T. Rojo, D.R. MacFarlane, M. Forsyth, P.C. Howlett, Controlling the three-phase boundary in Na–oxygen batteries: the synergy of carbon nanofibers and ionic liquid, ChemSusChem 12 (2019) 4054–4063, https://doi.org/10.1002/cssc.201901351.

[44] Z.E.M. Reeve, C.J. Franko, K.J. Harris, H. Yadegari, X. Sun, G.R Goward, Detection of electrochemical reaction products from the sodium-oxygen cell with solid-state ^{23}Na NMR spectroscopy, J. Am. Chem. Soc. 139 (2017) 595–598, https://doi.org/10.1021/jacs.6b11333.

[45] L. Gao, J. Chen, Y. Liu, Y. Yamauchi, Z. Huang, X. Kong, Revealing the chemistry of an anode-passivating electrolyte salt for high rate and stable sodium metal batteries, J. Mater. Chem. A 6 (2018) 12012–12017, https://doi.org/10.1039/c8ta03436b.

[46] M. Hayyan, M.A. Hashim, I.M. Alnashef, Superoxide ion: generation and chemical implications, Chem. Rev. 116 (2016) 3029–3085, https://doi.org/10.1021/acs.chemrev.5b00407.

[47] M. Enterría, M. Reynaud, J.I. Paredes, L. Medinilla, R. Younesi, N. Ortiz-Vitoriano, Driving the sodium-oxygen battery chemistry towards the efficient formation of discharge products: the importance of sodium superoxide quantification, J. Energy Chem. 68 (2022) 709–720, https://doi.org/10.1016/j.jechem.2021.12.014.

[48] R. Black, A. Shyamsunder, P. Adeli, D. Kundu, G.K. Murphy, L.F. Nazar, The nature and impact of side reactions in glyme-based sodium–oxygen batteries, ChemSusChem 9 (2016) 1795–1803, https://doi.org/10.1002/cssc.201600034.